Rising geopotential height under global warming

Chao He (hechao@jnu.edu.cn)
Jinan University https://orcid.org/0000-0001-5842-9617
Xiaolong Chen
Institute of Atmospheric Physics Chinese Academy of Sciences
Matthew Collins
University of Exeter
Fengfei Song
Ocean University of China
Yamin Hu
China Meteorological Administration
Xingwen Jiang
China Meteorological Administration
Yanju Liu
China Meteorological Administration
Yihui Ding
China Meteorological Administration
Wen Zhou
Fudan University

Research Article

Keywords: geopotential height, global warming, thermal expansion, hypsometric equation

Posted Date: October 6th, 2023

DOI: https://doi.org/10.21203/rs.3.rs-3390987/v1

Rising geopotential height under global warming

Chao He[1]*, Xiaolong Chen[2], Matthew Collins[3], Fengfei Song[4], Yamin Hu[5], Xingwen Jiang[6], Yanju Liu[7], Yihui Ding[7], Wen Zhou[8]

1. Institute for Environmental and Climate Research, Jinan University, Guangzhou, China
2. LASG, Institute of Atmospheric Physics, Chinese Academy of Sciences, Beijing, China
3. College of Engineering, Mathematics and Physical Sciences, University of Exeter, Exeter, UK
4. Frontier Science Centre for Deep Ocean Multispheres and Earth System and Physical Oceanography Laboratory, Ocean University of China, Qingdao, China
5. Guangdong Climate Center, China Meteorological Administration, Guangzhou, China
6. Institute of Plateau Meteorology, China Meteorological Administration, Chengdu, China
7. National Climate Center, China Meteorological Administration, Beijing, China
8. Department of Atmospheric and Oceanic Sciences & Institute of Atmospheric Sciences, Fudan University, Shanghai, China

Submitted to ***Climate Dynamics***

*Email Address: hechao@jnu.edu.cn

Abstract

Geopotential height (H) is a widely used metric for atmospheric circulation. H has been reported to be rising under global warming, but the amplitude and mechanism of this rise are not clear. Based on reanalysis datasets and climate models participating in CMIP6, this study quantitatively evaluates the sensitivity of H to global mean surface air temperature (T_s), i.e., $\mathrm{d}H/\mathrm{d}T_s$. Reanalysis datasets and model simulations consistently show that $\mathrm{d}H/\mathrm{d}T_s$ increases monotonically with altitude in the troposphere, with a global averaged value of about 24.5 gpm/K at 500 hPa, which overwhelms the interannual H variability. Diagnosis based on the hypsometric equation shows that the rise in H is dominated by temperature-driven expansion, i.e., expansion of the air column due to warming-induced reduction of air density, while moisture-driven expansion and the surface pressure effect play only minor roles. Therefore, the magnitude of $\mathrm{d}H/\mathrm{d}T_s$ is determined largely by a vertical integration of the warming profile below the pressure level. Since the anthropogenic forced rise in H is rather horizontally uniform and proportional to T_s change, past and projected future changes in the global H field at each pressure level can be reproduced by change in T_s multiplied by a constant historical $\mathrm{d}H/\mathrm{d}T_s$ value. The spatially uniform rise in H reproduces the past and projected future expansion of the widely used H=5880 gpm contour at 500 hPa, suggesting that it does not indicate enhancement of the subtropical high but is simply caused by thermal expansion of the atmosphere.

Keywords: geopotential height, global warming, thermal expansion, hypsometric equation

1. Introduction

Geopotential height (*H*) is a widely used variable in meteorology. It is key in generating daily weather charts, and it is also a useful metric for the variability of atmospheric circulation, particularly high and low pressure systems (e.g., Sickmöller et al. 2000; Chan et al. 2019; Pedatella and Harvey 2022; Sharma et al. 2022), and ridges and troughs (Wang et al. 2009; Mishra et al. 2012; Liu et al. 2018; Zhang et al. 2022a). A positive *H* anomaly usually indicates an anomalously strong high pressure (or ridge) system or an anomalously weak low pressure (or trough) system (e.g., Wei et al. 2014; Bowerman et al. 2017; Kawasaki et al. 2021). Characteristic contours of *H* are also widely adopted to define the boundary of a pressure system. For example, the *H*=5880 gpm contour at 500 hPa is widely used as the boundary of subtropical high pressure systems in the mid-troposphere, such as the western North Pacific subtropical high (WNPSH, e.g., Li et al. 2021; Nie et al. 2022; Yang et al. 2023; Tang et al. 2023; Zhang et al. 2023) and the Iran high (e.g., Ninomiya and Kobayashi 1998; Rasul et al. 2005; Mashat et al. 2021; Chen et al. 2023; Zhang et al. 2023), and the *H*=12500 gpm contour at 200 hPa is widely used as the boundary of the South Asian high (e.g., Sugimoto and Ueno 2012; Wei et al. 2014; Choi et al. 2015; Wang and Wang 2021; Cha et al. 2021; Zhang et al. 2023) in the upper troposphere.

Since *H* is an important metric for atmospheric circulation systems, it is important to investigate long-term changes in the global *H* field. A rising trend in *H* has been noted by many studies, based on multiple reanalysis datasets (Yang and Sun 2003; Hafez and Almazroui 2014; Huang et al. 2015; Wu and Wang 2015) and climate model simulations under increasing greenhouse gas forcing (Liu et al. 2014; Christidis and Stott 2015; He et al. 2015; Sun et al. 2022). It appears that the rise in *H* under global warming is a global phenomenon that can be attributed to forcing by anthropogenic greenhouse gases (Christidis and Stott 2015). The amplitudes of the rising trends in *H* differ among pressure levels, and it seems that *H* is rising more rapidly in the upper troposphere than in the middle and lower troposphere (Nassif et al. 2020). However, there is still no global-scale quantitative evaluation on the amplitude of the rise in *H* under global warming, and it is unclear what determines the amplitude of this rise at each pressure level.

By definition, *H* at a given pressure level *P* is the height (in units of gpm) of the top of an air column between the land/ocean surface and the pressure level *P*. The top of the air column may rise if the entire air column is lifted upward (schematically shown in the left-hand portion of Fig. 1) or the length of the air column increases (schematically shown in the right-hand portion of Fig. 1). As a result of increasing atmospheric water vapor content under global warming (Trenberth and Smith 2005; Yang et al. 2016; Allan et al. 2022; Borger et al. 2022), global total air mass is increasing and leading to an overall increase in surface pressure, which acts to lift the air column upward and increases the *H* value for the air column even if the length of the air column is fixed. On the other hand, the length of an air column is inversely proportional to air density, assuming the air column has a fixed mass content, and the top of an air column may rise if the length of the air column increases due to reduced air density. Since warmer and moister air has lower density, air density can be reduced by rising temperature (Ren et al. 2018; Zhou et al. 2018; Ren et al. 2023) and increased atmospheric moisture content under global warming (Trenberth and Smith 2005; Held and Soden 2006; Borger et al. 2022). The above factors may act to increase *H*, but the relative contribution of each is unclear.

Observational evidence suggests a substantial expansion of the areal coverage of characteristic contours of *H* in recent decades, such as the *H*=5880 gpm contour at 500 hPa, which has been interpreted as an expansion and enhancement of the subtropical high (e.g., Yan et al. 2011; Sun and Li 2018; Lee et al. 2021; Li et al. 2021). Meanwhile, an "extremely strong" subtropical high has frequently been reported in recent years. For example, the summertime WNPSH was reported to be exceptionally strong and extended farther westward than normal in 2020 (e.g., Takaya et al. 2020; Qiao et al. 2021; Zhou et al. 2021; Shi and Fang 2022), as well as in 2021 (Ke et al. 2022; Ma et al. 2022; Zhang et al. 2022b) and 2022 (Chen and Li 2023; Li et al. 2023; Zhang et al. 2023). In the summer of 2022, maybe for the first time, the characteristic contour of *H*=5880 gpm covered the Tibetan Plateau and encircled the globe, possibly indicating an extremely strong subtropical high and drawing wide attention from the research community (Mallapaty 2022; Chen and Li 2023; Zhang et al. 2023).

The frequent occurrence of an "exceptionally strong" subtropical high in recent years may be connected to a long-term trend, because recent years are compared with the past "climate normal" during real-time climate monitoring and extreme event attribution. If a variable has a substantial positive (negative) trend, it may bias the "anomaly" in recent years toward a positive (negative) value based on such comparison (Livezey et al. 2007; Arguez and Vose 2011), similar to the well-known fact that warm anomalies are more frequent and stronger than cold anomalies due to the rising temperature trend (Hulme et al. 2009; Rahmstorf and Coumou 2011; Hansen et al. 2012; Lorenz et al. 2019). The long-term expansion of the characteristic *H*=5880 gpm contour is robust in observational records (e.g., Yan et al. 2011; Sun and Li 2018; Li et al. 2021) and also in future climate projection experiments (Liu et al. 2014), but it is still uncertain whether this suggests expansion and enhancement of the subtropical high (He et al. 2015, 2018; Huang and Li 2015;

Huang et al. 2015; Wu and Wang 2015). By definition, two factors may result in the expansion of the characteristic H contour. One is a uniform rise in global H, which has no relation to atmospheric circulation, and the other is a pattern change in the H field, which is associated with change in circulation. It is unclear which factor dominates the past and projected future changes in the H field and the characteristic contour.

This study focuses on the sensitivity of H to global mean surface air temperature (T_s) and addresses the following two questions: 1) How strong is the response of H at each pressure level to T_s warming, and what determines the amplitude of dH/dT_s? 2) What controls the past and projected future change in the global H field and the characteristic contours of H? To address these two questions, Section 2 introduces the data and methods. Section 3 quantitatively evaluates dH/dT_s and the mechanism controlling its amplitude, and tries to constrain the past and projected future change in H based on the temporal evolution of T_s. Section 4 summarizes the major findings.

2. Data and Methods

2.1. Reanalysis and model data

In this study, the observed global mean surface air temperature (T_s) is based on the Met Office Hadley Centre observation dataset version 5 (Morice et al. 2021), spanning from 1850 to 2022. Five reanalysis datasets are also adopted in this study: 1) the ERA5 reanalysis (Hersbach et al. 2020; Bell et al. 2021), 2) the NCEP-NCAR reanalysis (NCEP1, Kalnay et al. 1996), 3) the NCEP-DOE reanalysis version 2 (NCEP2, Kanamitsu et al. 2002), 4) the Japanese 55-year Reanalysis (JRA55, Kobayashi et al. 2015), and 5) the Modern-Era Retrospective Analysis for Research and Applications, version 2 (MERRA2, Gelaro et al. 2017). Since the ERA5 dataset has a long temporal coverage from 1940 to 2022, it is the main reanalysis dataset analyzed in this work. The other four reanalysis datasets have relatively short temporal coverage, and we use the common period of 1980-2022 for these four datasets to address the uncertainty among the reanalysis datasets (Collins et al. 2013; Simmons et al. 2017; Ramon et al. 2019).

In order to extract the anthropogenic forced signal, this work uses monthly outputs of the historical, SSP1-2.6, SSP2-4.5, and SSP5-8.5 experiments based on 40 coupled climate models (the SSP1-2.6 experiment is unavailable for 3 of the 40 models) participating in the 6th phase of the Coupled Model Intercomparison Project (CMIP6). The historical experiment is forced by observed year-to-year concentrations of external forcing agents (greenhouse gases, aerosols, etc.) until 2014, and the SSP1-2.6, SSP2-4.5, and SSP5-8.5 experiments are performed under low, moderate, and high emission scenarios from 2015 to the end of the 21st century, in which the radiative forcing reaches 2.6, 4.5, and 8.5 W/m^2 until the year 2100 (Eyring et al. 2016; O'Neill et al. 2016). The first realization ("r1i1p1f1") of each model is selected by default, and another realization is selected if "r1i1p1f1" is unavailable or missing key variables. The names of the models and realizations adopted are listed in Supplementary Table S1. We focus on boreal summer in this study, and all the monthly reanalysis and model data are converted into June-July-August (JJA) mean values and interpolated onto a common 1°×1° grid.

2.2. Method

In order to examine the rise in H and its dependence on T_s, we quantify the rise in H under global warming as the linear regression slope of H onto T_s based on the 83 summers from 1940 to 2022 (denoted as dH/dT_s), similar to previous studies (e.g., Held and Soden 2006; Mishra et al. 2012; Zhou and Wang 2017), which indicates the amplitude of the rise in H corresponding to 1 K of T_s warming. Here, T_s is the time series of global mean surface air temperature, while H refers to either a 2-D geopotential height field or the global averaged value at a pressure surface. As the historical experiment terminates in 2014, we extend it to 2022 using the SSP2-4.5 experiment in order to match the temporal coverage of the ERA5 reanalysis data. The dH/dT_s value for each model is calculated based on the 1940~2022 period, and the multi-model mean (MMM) value among all available models represents the anthropogenic forced signal.

For large-scale motion, hydrostatic equilibrium requires the vertical pressure gradient force to balance the gravity force,

$$\frac{\mathrm{d}P}{\mathrm{d}H} = -\rho g \tag{1}$$

where P, ρ, and H are the air pressure, density, and geopotential height, respectively, and g=9.80665 m/s^2 is gravitational acceleration (globally constant g is assumed in this study). Inverting Eq. (1) into $\mathrm{d}H/\mathrm{d}P = -1/(\rho g)$ and integrating it from the surface (P_s) to pressure level P, the length of the air column can be expressed as

$$H(P) - H_s = \frac{1}{g}\int_{Ps}^{P}\frac{1}{\rho}\,\mathrm{d}p' \tag{2}$$

where $H(P)$ is the geopotential height at pressure level P, and H_s is the geopotential height of the surface determined by topography. Eq. (2) shows that the geopotential height at pressure level P may increase if: 1) the length of the air column increases due to reduced air density (ρ), or 2) the entire air column is lifted upward due to increased surface pressure P_s. This is consistent with the schematic illustration in Fig. 1.

The density of air depends on pressure and virtual temperature via the equation of state,

$$P=\rho R_d T_v \tag{3}$$

where R_d=287 J/(kg·K) is the constant of dry air, and virtual temperature T_v is a function of temperature T and specific humidity q, i.e., T_v=(1+0.608q)T. Eliminating ρ in Eq. (2), we obtain

$$H(P)= H_s+\frac{R_d}{g}\int_P^{P_s}(1+0.608q)\,\frac{T}{p'}\,\mathrm{d}p' \tag{4}$$

Eq. (4) states that H at a pressure level P is a function of temperature (T), specific humidity (q), and surface pressure (P_s), i.e., H=H(T, q, P_s). Based on the temperature, specific humidity, and surface pressure data, Eq. (4) well reconstructs the climatological H field (Supplementary Fig. S1) and the H field for an individual year (Supplementary Fig. S2). As T, q, and P_s may change under global warming, the response of H to global warming can be decomposed as the sum of these three contributing factors based on the chain rule

$$\frac{\mathrm{d}H}{\mathrm{d}T_s}=\frac{\partial H}{\partial T}\frac{\mathrm{d}T}{\mathrm{d}T_s}+\frac{\partial H}{\partial q}\frac{\mathrm{d}q}{\mathrm{d}T_s}+\frac{\partial H}{\partial P_s}\frac{\mathrm{d}P_s}{\mathrm{d}T_s} \tag{5}$$

We name the three terms on the right-hand-side of Eq. (5) T-driven expansion, q-driven expansion, and the P_s effect, which arise from changes in temperature, moisture, and surface pressure, respectively. Each of these three terms is estimated by artificially reconstructing the year-to-year H value based on Eq. (4) with the other two contributing factors fixed. For example, synthetic H in each year is reconstructed based on Eq. (4) using actual year-to-year T values and climatological q and P_s values, and the regression slope of it onto T_s is the contribution of T-driven expansion to the rise in H. Similarly, the contribution of q-driven expansion (P_s effect) is estimated by retaining q (P_s) variability and fixing the other two factors.

3. Results

3.1 Magnitudes of dH/dT_s and the contributing factors

Fig. 2a shows dH/dT_s at 500 hPa based on the ERA5 data, and Fig. 2b-d shows the contributions of the three terms in Eq. (5). It is obvious that H rises globally, with a global average of 23.1 gpm/K (Fig. 2a). The amplitude of the rise in H is rather smooth in the tropics but shows a wavy pattern in the mid-latitudes. T-driven expansion contributes the most to the rise in H, with a global average of 20.2 gpm/K (Fig. 2b), accounting for about 90% of the total rise in H. Although global moisture content increases (Trenberth and Smith 2005; Borger et al. 2020; Allan et al. 2022), the consequent q-driven expansion contributes only 0.7 gpm/K (Fig. 2c), and its effect on H can be neglected. The P_s effect acts to increase H over plateau regions and the subtropical Southern Hemisphere but reduces H over subpolar regions in the Southern Hemisphere, which amounts to a global averaged value of 2.2 gpm/K (Fig. 2d). The sum of the three terms (Fig. 2e) shares a very similar spatial pattern and global averaged amplitude (23.1 gpm/K) with $\mathrm{d}H/\mathrm{d}T_s$ as shown in Fig. 2a. Evidently, T-driven expansion dominates most of the rise in H in recent decades by reducing air density. The column-averaged change in temperature between the surface and 500 hPa (Fig. 2f) shows a very similar pattern to T-driven expansion (Fig. 2b), suggesting that a larger (smaller) rise in H occurs where there is stronger (weaker) warming.

The anthropogenic forced $\mathrm{d}H/\mathrm{d}T_s$ at 500 hPa based on the MMM of 40 models shows a positive trend at all grid points (Fig. 3a), with a global average of 24.5 gpm/K. The MMM-simulated $\mathrm{d}H/\mathrm{d}T_s$ has a much smoother spatial pattern compared with that based on the ERA5 data, but the global averaged values are very close to each other, suggesting that the discrepancy in spatial pattern may result from internal climate variability in recent decades such as the southern/northern annualar mode (Baldwin 2001; Marshall 2003; Visbeck 2009). Based on the MMM, T-driven expansion also explains about 90% of the anthropogenic forced rise in H, while q-driven expansion and the P_s effect play minor roles (Fig. 3b-d). The sum of the three contributing factors (Fig. 3e) accurately reconstructs the spatial pattern and magnitude of $\mathrm{d}H/\mathrm{d}T_s$ (Fig. 3a). A higher rate of $\mathrm{d}H/\mathrm{d}T_s$ near the North Pole (Fig. 3a) is reproduced by the T-driven expansion (Fig. 3b). Indeed, the anthropogenic forced increase in temperature is greater near the North Pole (Fig. 3f) known as "polar amplification" (e.g., Holland and Bitz 2003; Bekryaev et al. 2010; Stuecker et al. 2018; Chylek et al. 2022), and it results in a stronger reduction in air density and larger T-driven expansion near the North Pole under anthropogenic forcing.

We also use the amplitude of the interannual H variability as a benchmark and compare it with the magnitude of $\mathrm{d}H/\mathrm{d}T_s$, similar to the concept of the "signal-to-noise" ratio (Chen et al. 2020; Auger et al. 2021; Ying et al. 2022). A 9-year high-pass Fourier filter is applied to the time series of H at each grid point before the standard deviation ($\sigma(H)$) is calculated. The MMM and ERA5 dataset consistently show that $\sigma(H)$ is below 10 gpm in the tropics and increases with latitude (Fig. 4a). The ratio between $\mathrm{d}H/\mathrm{d}T_s$ and $\sigma(H)$ is above 4 in the deep tropics (Fig. 4b), and the tropical (30°S-30°N) averaged ratio is 3.9, suggesting that the increase in H per 0.25 K of warming is comparable with the amplitude of interannual H variability in the tropics. The magnitude of $\mathrm{d}H/\mathrm{d}T_s$ is also greater than $\sigma(H)$ over the mid- to high latitudes in the Northern Hemisphere, and the global averaged ratio between $\mathrm{d}H/\mathrm{d}T_s$ and $\sigma(H)$ reaches 2.6. Since geostrophic wind proportional to the horizontal gradient of H is a good approximation of atmospheric circulation off the equator, we calculate the meridional and zonal gradients of H, i.e., $H_y=\partial H/\partial y$ and $H_x=\partial H/\partial x$, to measure the associated change in atmospheric circulation. As shown in Fig. 4c,d, the anthropogenic forced changes in the H gradient (both H_y and H_x) with T_s are one order of magnitude smaller than the amplitude of interannual variability, suggesting that the rise in H under global warming is rather spatially uniform and has little relation to changes in the H gradient and atmospheric circulation.

Since the anthropogenic forced rise in H is rather spatially uniform, we focus primarily on the global average. In the following discussion, the terms "H" and "dH/dT_s" refer to the global averaged values unless otherwise stated. To take into account the uncertainty among the reanalysis datasets (Collins et al. 2013; Simmons et al. 2017; Ramon et al. 2019), the global averaged values of dH/dT_s are calculated based on multiple reanalysis datasets and are shown in Table 1 and Fig. 5a. Obviously, dH/dT_s is positive throughout the troposphere and increases monotonically with altitude based on the MMM and all reanalysis datasets (Fig. 5a), indicating that it is a robust phenomenon that H in the upper troposphere is more sensitive to T_s warming than in the lower troposphere. The MMM-simulated dH/dT_s lies within the range based on reanalysis datasets in the lower and middle troposphere, but the MMM shows a larger dH/dT_s value in the upper troposphere than the reanalysis datasets (Fig. 5a). At 500 hPa, the dH/dT_s value is about 24 gpm/K for both the MMM and all reanalysis datasets. At 200 hPa, the dH/dT_s value reaches 62.1 gpm/K based on the MMM, which is greater than all of the reanalysis datasets by about 10 gpm/K. The cause for this discrepancy in the upper troposphere will be addressed in the next subsection.

3.2 Explaining the vertical profile of d*H*/d*T*$_s$

Since T-driven expansion dominates the rise in H, we need to understand how the vertical profile of dH/dT_s is controlled by T-driven expansion. Suppose that the warming in the troposphere follows a vertical profile $\Gamma(P)$ such that the amplitude of warming at level P can be expressed by the surface warming, i.e., $\Delta T(P) = \Gamma(P)\cdot\Delta T_s$. Neglecting the contribution of moisture to air density in Eq. (4), the rise in H (ΔH) due to T-driven expansion can be expressed as

$$\Delta H(P) = \varepsilon(P)\cdot\Delta T_S \tag{6}$$

where

$$\varepsilon(P) = \frac{R_d}{g}\int_P^{P_S}\frac{\Gamma(P)}{p'}\,\mathrm{d}p' \tag{7}$$

This relationship suggests that the amplitude of rise in H is proportional to the amplitude of rise in T_s, and the scaling factor is determined by the vertical integrated warming profile below the pressure level. Fig. 5b shows the vertical profile of $\varepsilon(P)$. In general, $\varepsilon(P)$ reproduces $\mathrm{d}H/\mathrm{d}T_s$ in terms of magnitude and vertical shape, suggesting that $\mathrm{d}H/\mathrm{d}T_s$ is determined largely by the vertical accumulated T-driven expansion below the pressure level. $\varepsilon(P)$ also largely reproduces the discrepancy in the $\mathrm{d}H/\mathrm{d}T_s$ values among the reanalysis datasets and the MMM. For example, the ε value at 200 hPa based on the MMM is greater than in all of the reanalysis datasets (Fig. 5b), which is consistent with the higher $\mathrm{d}H/\mathrm{d}T_s$ value at 200 hPa than in the reanalysis datasets (Fig. 5a), suggesting that the discrepancy results from the different vertical profiles of warming between the models and the reanalysis.

Fig. 5c,d shows the vertical profiles of warming (Γ) and the fractional change in air density due to T-driven expansion. Corresponding to surface air warming by 1 K, the troposphere warms by about 0.8~1.4K below 300 hPa (Fig. 5c), and the air density decreases by about 0.3~0.6% (Fig. 5d). Compared with the reanalysis datasets (colored curves in Fig. 5c), the MMM shows a greater warming in the mid-to-upper troposphere (black curve in Fig. 5c), which has already been noted in previous studies (Fu et al. 2011; Santer et al. 2017; Po-Chedley et al. 2021). Associated with the stronger mid-to-upper tropospheric warming, the MMM shows a larger decrease in air density in the mid-to-upper troposphere (Fig. 5d). Since the $\mathrm{d}H/\mathrm{d}T_s$ value on a given pressure level is determined largely by the accumulated T-driven expansion below the pressure level, the stronger mid-to-upper tropospheric warming explains the greater $\mathrm{d}H/\mathrm{d}T_s$ in the upper troposphere based on the MMM. Further study is needed to address the possible cause for the discrepancy in the vertical profile of warming between climate models and the reanalysis datasets (Santer et al. 2017; Po-Chedley et al. 2021).

3.3 Relating past and future evolution of H to T_s change

The curves in Fig. 6a and Fig. 6b show the time series of the T_s anomaly (ΔT_s) relative to the 1850-1899 baseline period and H at 500 hPa as global averages, based on observations and the MMM. It is clear that the temporal evolution of H resembles the evolution of ΔT_s, in terms of both past changes and projected future changes under multiple scenarios. Since the above evidence indicates that change in H is almost proportional to change in T_s, we reconstruct the temporal evolution of H based on the time series of ΔT_s. Based on the MMM of the models, the climatological H value for the baseline period is 5666.0 gpm and the $\mathrm{d}H/\mathrm{d}T_s$ value is 24.5 gpm/K at 500 hPa, so we show $5666.0+24.5\Delta T_s$ as hollow circles in Fig. 6b. It is clear that the reconstructed H accurately matches the temporal evolution of H in terms of past changes and projected future changes under all three scenarios, and it also matches the decadal change in H from 1940 to 2022 based on ERA5 dataset despite some internal variability.

Based on the MMM-projected changes in H (ΔH) and ΔT_s in each year from 2015 to 2099 under the three scenarios relative to the baseline (1850-1899) period, Fig. 7 further shows the ΔH value at each pressure level as a function of ΔT_s. At each pressure level, the (ΔH, ΔT_s) pairs are located along the $\Delta H = k\Delta T_s$ lines (thin black lines in Fig. 6) where k is the $\mathrm{d}H/\mathrm{d}T_s$ value at the pressure level listed in Table 1. For example, the projected future change in H at 500 hPa (200 hPa) can be approximated by ΔH=24.5ΔT_s (ΔH=62.1ΔT_s) according to the ΔT_s value under all three scenarios. A rise in T_s of 1.5 K (2.0 K) relative to the baseline period results in a rise in global H of about 37 gpm (49 gpm) at 500 hPa, which is consistent among the SSP1-2.6, SSP2-4.5, and SSP5-8.5 scenarios (Fig. 7a), and it can be simply reproduced as ΔH=24.5ΔT_s. This also confirms that future change in H at each pressure level is dominated by the amplitude of T_s warming, and it offers a simple way to estimate the change in global H based on the amplitude of T_s warming.

The H=5880 gpm contour at 500 hPa, which has been widely used as the boundary of the subtropical high in the mid-troposphere (see Supplementary Figs. S1, S2), has expanded substantially in the past decades (e.g., Yan et al. 2011; Sun and Li 2018; Lee et al. 2021; Li et al. 2021) and is projected to continue expanding in the future (Liu et al. 2014). Here, we define an area index (AI) as the number of global grid points (on a 1°×1° grid) with an H value above 5880 gpm, shown as curves in Fig. 6c. The expansion of this contour may be induced by either a uniform rise in H or a pattern change in the H field. In order to assess the effect of the uniform rise in H on the increase of AI, we reconstruct an idealized evolution of global H field by adding a global uniform value of 24.5ΔT_s (unit: gpm) according to the ΔT_s value in each year to the climatological H field of the baseline period, i.e., $H_c(x,y)$+24.5ΔT_s, where $H_c(x,y)$ is the climatological H field of the baseline period. Based on such a reconstructed temporal evolution of H field subject to a global uniform rising trend, a reconstructed AI is calculated and shown as hollow circles in Fig. 6c. The hollow circles and the curves almost overlap each other in Fig. 6c for historical experiment and all scenarios, suggesting that the historical and future evolution of AI can be accurately reproduced by the reconstruction subject to a global uniform rise in H. The residual of the reconstruction associated with change in H pattern is small and negligible (figure not shown). This suggests that the expansion of the H=5880 gpm contour is driven primarily by thermal expansion of the atmosphere and has little relation to atmospheric circulation.

Unlike the linear relationship between H and T_s, AI has a nonlinear relation with ΔT_s (Fig. 7b). AI increases sharply with ΔT_s when ΔT_s is below 1.8 K, and the increase in AI is moderate when ΔT_s exceeds 1.8K (Fig. 7b). By definition, the sensitivity of AI to T_s depends on the number of additional grid points whose H values reach the threshold of 5880 gpm. Overall, the H value is higher in tropics than mid-high latitudes (see Supplementary Fig. S1), and the H gradient is weak in the tropics due to the weak temperature gradient (Sobel et al. 2001; Polvani and Sobel 2002; Su et al. 2003). There is a large number (about 10^4) of tropical grid points with an H value within the 5840~5860 gpm interval (Fig. 8a), just slightly below the threshold of 5880 gpm. Since the rise in H is rather spatially uniform, the amplitude of T_s warming required for the H value to exceed 5880 gpm at a given grid point can be estimated as $(5880-H)/24.5$, by assuming a dH/dT_s value of 24.5gpm/K at 500 hPa. As shown in Fig. 8b, the H values at a large number of additional grid points (mostly in tropics) exceed the 5880 gpm threshold under a ΔT_s of 1.3~1.8K (Fig. 8b), which is consistent with the period of rapid increase in AI in the 2020s and 2030s (Fig. 6c and Fig. 7b). Therefore, a global uniform rise in H at a constant rate of 24.5 gpm/K explains the nonlinear rise of the AI, with the rate of rising controlled by the pattern of climatological H field.

Many previous studies suggested an enhancement and expansion of the subtropical high (e.g., Yan et al. 2011; Sun and Li 2018; Lee et al. 2021; Li et al. 2021), based on the characteristic contour of H=5880 gpm (or another contour) since it is widely used as the boundary of subtropical high, but there is still debate about the long-term change in the subtropical high because other circulation-based metric does not show such a phenomenon (Huang et al. 2015; Shaw and Voigt 2015; Wu and Wang 2015; He et al. 2017; Cherchi et al. 2018; He and Zhou 2022). Based on our above results, the expansion of the characteristic contour primarily results from a global uniform rising trend of H, and it is not related to change in atmospheric circulation. Meanwhile, the rising trend of H may, at least partly, be responsible for the frequent occurrence of "extremely strong" subtropical high events in recent years, such as the extremely strong WNPSH events in 2020 (e.g., Takaya et al. 2020; Qiao et al. 2021; Zhou et al. 2021; Shi and Fang 2022), 2021 (Ke et al. 2022; Ma et al. 2022; Zhang et al. 2022b) and 2022 (Chen and Li 2023; Li et al. 2023; Tang et al. 2023; Zhang et al. 2023) based on H anomaly or characteristic H contour. This is because a recent year is compared with a "climate normal" based on past decades in attribution studies, and the strong rising trend of H may push the H anomaly (and also the anomalous AI for subtropical high) in recent years toward a positive anomaly in comparison to a past "climate normal" (Livezey et al. 2007; Arguez and Vose 2011; Rahmstorf and Coumou 2011; Hansen et al. 2012). More comparison among different metrics is needed in the explanation of extreme climate events from atmospheric circulation perspective.

4. Summary

Previous studies have noted a rising trend in H under global warming, and this work quantitatively evaluates the rise in H in the troposphere in terms of its sensitivity to T_s warming, based on multiple reanalysis datasets and climate models participating in CMIP6. Reanalysis data and climate models consistently show that it is a global phenomenon that H rises under global warming, and the amplitude of rise in H increases monotonically with altitude in the troposphere due to vertically accumulated thermal expansion. As a global average, H at 500 hPa rises at a rate of 24.5 gpm/K due to anthropogenic forcing, which is about 4 times the amplitude of interannual H variability in the tropics. The anthropogenic forced rise in H is rather spatially uniform, and the associated change in the horizontal gradient of H is one order of magnitude smaller than its interannual variability, suggesting that the rise in H has little relation to atmospheric circulation.

Based on the hypsometric equation, this work identifies three contributing factors to the rise of H. They include T-driven expansion, q-driven expansion, and the P_s effect, which indicate the roles of temperature, moisture, and surface pressure, respectively. Diagnosis based on the hypsometric equation shows that the T-driven expansion of the air column explains a major fraction (about 90%) of the increase in H by reducing air density, while the effects of q-driven expansion and a general increase in global surface pressure play minor roles. Given the dominant role of T-driven expansion, the amplitude and vertical structure of $\mathrm{d}H/\mathrm{d}T_s$ can be approximated based on a vertical integration of the warming profile, which physically indicates the accumulated expansion of the air column below the pressure level.

Since the anthropogenic forced change in H is rather uniform and the global averaged change in H is almost proportional to the change in T_s, the past and projected future changes in H can be accurately reproduced by the evolution of T_s based on a simple linear relationship. The H=5880 gpm contour at 500 hPa, which is widely used as the boundary for the subtropical high, has expanded substantially under global warming. This phenomenon has drawn great attention from the research community regarding a rapid enhancement of the subtropical high and the recent frequent occurrence of "exceptionally strong" subtropical high events (e.g., Liu et al. 2014; Mallapaty et al. 2022; Chen and Li 2023; Zhang et al. 2023). Our results show that the past and projected future expansion of the contour can be accurately reproduced by assuming a global uniform rise in H of 24.5 gpm/K, suggesting that the expansion of the characteristic contour is dominated by a uniform rise in H rather than a change in H pattern and circulation. Therefore, thermal expansion of the atmosphere is responsible for the expansion of the characteristic contour and it does not suggest enhancement of the subtropical high.

Funding

This work was supported by Guangdong Major Project of Basic and Applied Basic Research (2020B0301030004) and the National Natural Science Foundation of China (42175024).

Author Contributions

C. H. performed data analysis and wrote the initial draft of the manuscript. All authors contributed to design the study and improve the manuscript.

Data Availability Statements

All the datasets adopted in this study can be accessed online via the following URLs.

1. CMIP6 model data

https://esgf-node.llnl.gov/search/cmip6

2. Met Office Hadley Centre global historical surface temperature version 5 (HadCRUT5)

https://www.metoffice.gov.uk/hadobs/hadcrut5

3. ERA5 global gridded monthly reanalysis data (ERA5)

https://cds.climate.copernicus.eu/cdsapp#!/dataset/reanalysis-era5-pressure-levels-monthly-means

4. NCEP/NCAR reanalysis (NCEP1)

https://psl.noaa.gov/data/gridded/data.ncep.reanalysis.html

5. NCEP/DOE reanalysis version 2 (NCEP2)

https://psl.noaa.gov/data/gridded/data.ncep.reanalysis2.html

6. Japanese 55-year reanalysis (JRA55)

https://rda.ucar.edu/datasets/ds628.1/dataaccess

7. Modern-Era Retrospective Analysis for Research and Applications (MERRA2)

https://disc.gsfc.nasa.gov/datasets?project=MERRA-2

Declarations

The authors declare no conflicts of interest or competing interests.

References

Allan RP, Willett KM, John VO, Trent T (2022) Global Changes in Water Vapor 1979–2020. Journal of Geophysical Research: Atmospheres 127 (12). doi:10.1029/2022jd036728

Arguez A, Vose RS (2011) The Definition of the Standard WMO Climate Normal: The Key to Deriving Alternative Climate Normals. B Am Meteorol Soc 92 (6):699-704. doi:10.1175/2010bams2955.1

Auger M, Morrow R, Kestenare E, Sallée J-B, Cowley R (2021) Southern Ocean in-situ temperature trends over 25 years emerge from interannual variability. Nature Communications 12 (1). doi:10.1038/s41467-020-20781-1

Baldwin MP (2001) Annular modes in global daily surface pressure. Geophys Res Lett 28 (21):4115-4118. doi:10.1029/2001gl013564

Bekryaev RV, Polyakov IV, Alexeev VA (2010) Role of Polar Amplification in Long-Term Surface Air Temperature Variations and Modern Arctic Warming. J Climate 23 (14):3888-3906. doi:10.1175/2010jcli3297.1

Bell B, Hersbach H, Simmons A, Berrisford P, Dahlgren P, Horányi A, Muñoz‐Sabater J, Nicolas J, Radu R, Schepers D, Soci C, Villaume S, Bidlot JR, Haimberger L, Woollen J, Buontempo C, Thépaut JN (2021) The ERA5 global reanalysis: Preliminary extension to 1950. Q J Roy Meteor Soc 147 (741):4186-4227. doi:10.1002/qj.4174

Borger C, Beirle S, Wagner T (2022) Analysis of global trends of total column water vapour from multiple years of OMI observations. Atmos Chem Phys 22 (16):10603-10621. doi:10.5194/acp-22-10603-2022

Bowerman AR, Fu R, Yin L, Fernando DN, Arias PA, Dickinson RE (2017) An influence of extreme southern hemisphere cold surges on the North Atlantic Subtropical High through a shallow atmospheric circulation. Journal of Geophysical Research: Atmospheres 122 (19). doi:10.1002/2017jd026697

Cha Y, Choi J, Kim E-S, Ahn J-B (2021) Occurrence of heatwave in Korea by the displacement of South Asian high. Clim Dynam 58 (5-6):1699-1718. doi:10.1007/s00382-021-05987-3

Chan P-W, Hassanzadeh P, Kuang Z (2019) Evaluating Indices of Blocking Anticyclones in Terms of Their Linear Relations With Surface Hot Extremes. Geophys Res Lett 46 (9):4904-4912. doi:https://doi.org/10.1029/2019GL083307

Chen L, Chen W, Hu P, Chen S, An X (2023) Climatological characteristics of the East Asian summer monsoon retreat based on observational analysis. Clim Dynam. doi:10.1007/s00382-022-06489-6

Chen R, Li X (2023) Causes of the persistent merging of the western North Pacific subtropical high and the Iran high during late July 2022. Clim Dynam. doi:10.1007/s00382-023-06678-x

Chen X, Zhou T, Wu P, Guo Z, Wang M (2020) Emergent constraints on future projections of the western North Pacific Subtropical High. Nature Communications 11 (1):2802. doi:10.1038/s41467-020-16631-9

Cherchi A, Ambrizzi T, Behera S, Freitas ACV, Morioka Y, Zhou T (2018) The Response of Subtropical Highs to Climate Change. Current Climate Change Reports 4 (4):371-382. doi:10.1007/s40641-018-0114-1

Choi K-S, Kim B-J, Zhang R, Nam J-C, Park K-J, Kim J-Y, Kim D-W (2015) Possible influence of South Asian high on summer rainfall variability in Korea. Clim Dynam 46 (3-4):833-846. doi:10.1007/s00382-015-2615-0

Christidis N, Stott PA (2015) Changes in the geopotential height at 500 hPa under the influence of external climatic forcings. Geophys Res Lett 42 (24):10,798-710,806. doi:10.1002/2015gl066669

Chylek P, Folland C, Klett JD, Wang M, Hengartner N, Lesins G, Dubey MK (2022) Annual Mean Arctic Amplification 1970–2020: Observed and Simulated by CMIP6 Climate Models. Geophys Res Lett 49 (13). doi:10.1029/2022gl099371

Collins M, Achutarao K, Ashok K, Bhandari S, Mitra AK, Prakash S, Srivastava R, Turner A (2013) Observational challenges in evaluating climate models. Nat Clim Chang 3:940-941

Eyring V, Bony S, Meehl GA, Senior CA, Stevens B, Stouffer RJ, Taylor KE (2016) Overview of the Coupled Model Intercomparison Project Phase 6 (CMIP6) experimental design and organization. Geoscientific Model Development 9 (5):1937-1958. doi:10.5194/gmd-9-1937-2016

Fu Q, Manabe S, Johanson CM (2011) On the warming in the tropical upper troposphere: Models versus observations. Geophys Res Lett 38 (15). doi:https://doi.org/10.1029/2011GL048101

Gelaro R, McCarty W, Suárez MJ, Todling R, Molod A, Takacs L, Randles CA, Darmenov A, Bosilovich MG, Reichle R, Wargan K, Coy L, Cullather R, Draper C, Akella S, Buchard V, Conaty A, da Silva AM, Gu W, Kim G-K, Koster R, Lucchesi R, Merkova D, Nielsen JE, Partyka G, Pawson S, Putman W, Rienecker M, Schubert SD, Sienkiewicz M, Zhao B (2017) The Modern-Era Retrospective Analysis for Research and Applications, Version 2 (MERRA-2). J Climate 30 (14):5419-5454. doi:10.1175/jcli-d-16-0758.1

Hafez YY, Almazroui M (2014) Recent Study of Anomaly of Global Annual Geopotential Height and

Global Warming. Atmospheric and Climate Sciences 04 (03):347-357. doi:10.4236/acs.2014.43035

Hansen J, Sato M, Ruedy R (2012) Perception of climate change. Proceedings of the National Academy of Sciences 109 (37):E2415-E2423. doi:doi:10.1073/pnas.1205276109

He C, Lin A, Gu D, Li C, Zheng B, Wu B, Zhou T (2018) Using eddy geopotential height to measure the western North Pacific subtropical high in a warming climate. Theor Appl Climatol 131 (1):681-691. doi:10.1007/s00704-016-2001-9

He C, Wu B, Zou L, Zhou T (2017) Responses of the Summertime Subtropical Anticyclones to Global Warming. J Climate 30 (16):6465-6479. doi:10.1175/jcli-d-16-0529.1

He C, Zhou T (2022) Distinct Responses of North Pacific and North Atlantic Summertime Subtropical Anticyclones to Global Warming. J Climate 35 (24):4517-4532. doi:10.1175/jcli-d-21-1024.1

He C, Zhou T, Lin A, Wu B, Gu D, Li C, Zheng B (2015) Enhanced or Weakened Western North Pacific Subtropical High under Global Warming? Scientific Reports 5:16771. doi:10.1038/srep16771

Held IM, Soden BJ (2006) Robust responses of the hydrological cycle to global warming. J Climate 19 (21):5686-5699. doi:10.1175/jcli3990.1

Hersbach H, Bell B, Berrisford P, Hirahara S, Horányi A, Muñoz‐Sabater J, Nicolas J, Peubey C, Radu R, Schepers D, Simmons A, Soci C, Abdalla S, Abellan X, Balsamo G, Bechtold P, Biavati G, Bidlot J, Bonavita M, Chiara G, Dahlgren P, Dee D, Diamantakis M, Dragani R, Flemming J, Forbes R, Fuentes M, Geer A, Haimberger L, Healy S, Hogan RJ, Hólm E, Janisková M, Keeley S, Laloyaux P, Lopez P, Lupu C, Radnoti G, Rosnay P, Rozum I, Vamborg F, Villaume S, Thépaut JN (2020) The ERA5 global reanalysis. Q J Roy Meteor Soc 146 (730):1999-2049. doi:10.1002/qj.3803

Holland MM, Bitz CM (2003) Polar amplification of climate change in coupled models. Clim Dynam 21 (3-4):221-232. doi:10.1007/s00382-003-0332-6

Huang Y, Li X (2015) The Interdecadal Variation of the Western Pacific Subtropical High as Measured by 500 hPa Eddy Geopotential Height Atmospheric and Oceanic Science Letters 8 (6):371-375. doi:10.3878/AOSL20150038

Huang Y, Wang H, Fan K, Gao Y (2015) The western Pacific subtropical high after the 1970s: westward or eastward shift? Clim Dynam 44 (7-8):2035-2047. doi:10.1007/s00382-014-2194-5

Hulme M, Dessai S, Lorenzoni I, Nelson DR (2009) Unstable climates: Exploring the statistical and social constructions of 'normal' climate. Geoforum 40 (2):197-206.

doi:10.1016/j.geoforum.2008.09.010

Kalnay E, Kanamitsu M, Kistler R, Collins W, Deaven D, Gandin L, Iredell M, Saha S, White G, Woollen J, Zhu Y, Chelliah M, Ebisuzaki W, Higgins W, Janowiak J, Mo KC, Ropelewski C, Wang J, Leetmaa A, Reynolds R, Jenne R, Joseph D (1996) The NCEP/NCAR 40-year reanalysis project. B Am Meteorol Soc 77 (3):437-471. doi:10.1175/1520-0477(1996)077<0437:tnyrp>2.0.co;2

Kanamitsu M, Ebisuzaki W, Woollen J, Yang SK, Hnilo JJ, Fiorino M, Potter GL (2002) NCEP-DOE AMIP-II reanalysis (R-2). B Am Meteorol Soc 83 (11):1631-1643. doi:10.1175/bams-83-11-1631

Kawasaki K, Tachibana Y, Nakamura T, Yamazaki K (2021) Role of the Cold Okhotsk Sea on the Climate of the North Pacific Subtropical High and Baiu Precipitation. J Climate 34 (2):495-507. doi:10.1175/jcli-d-20-0432.1

Ke M, Wang Z, Pan W, Luo H, Yang S, Guo R (2022) Extremely Strong Western Pacific Subtropical High in May 2021 Following a La Niña Event: Role of the Persistent Convective Forcing over the Indian Ocean. Asia-Pacific Journal of Atmospheric Sciences 59 (1):47-58. doi:10.1007/s13143-022-00300-6

Kobayashi S, Ota Y, Harada Y, Ebita A, Moriya M, Onoda H, Onogi K, Kamahori H, Kobayashi C, Endo H, Miyaoka K, Takahashi K (2015) The JRA-55 Reanalysis: General Specifications and Basic Characteristics. Journal of the Meteorological Society of Japan Ser II 93 (1):5-48. doi:10.2151/jmsj.2015-001

Lee H-J, Jeon W, Lee W-S, Lee HW (2021) Human-Perceived Temperature Changes in South Korea and Their Association with Atmospheric Circulation Patterns. J Climate 34 (4):1273-1290. doi:10.1175/jcli-d-20-0344.1

Li N, Xiao Z, Zhao L (2021) A Recent Increase in Long-Lived Heatwaves in China Under the Joint Influence of South Asia and Western North Pacific Subtropical Highs. J Climate:1-42. doi:10.1175/jcli-d-21-0014.1

Li Z, Xiao Z, Ling J (2023) Impact of extremely warm Tibetan Plateau in spring on the rare rainfall anomaly pattern in the regions west and east to Plateau in late summer 2022. Atmos Res 290:106797. doi:10.1016/j.atmosres.2023.106797

Liu K, Zha J, Yang R, Chen J (2018) A New Dynamical Index for India-Burma Trough. Advances in Meteorology 2018:1-10. doi:10.1155/2018/5215093

Liu Y, Li W, Zuo J, Hu Z-Z (2014) Simulation and projection of the western Pacific subtropical high in CMIP5 models. J Meteorol Res 28 (3):327-340. doi:10.1007/s13351-014-3151-2

Livezey RE, Vinnikov KY, Timofeyeva MM, Tinker R, van den Dool HM (2007) Estimation and Extrapolation of Climate Normals and Climatic Trends. Journal of Applied Meteorology and Climatology 46 (11):1759-1776. doi:doi:10.1175/2007JAMC1666.1

Lorenz R, Stalhandske Z, Fischer EM (2019) Detection of a Climate Change Signal in Extreme Heat, Heat Stress, and Cold in Europe From Observations. Geophys Res Lett 46 (14):8363-8374. doi:10.1029/2019gl082062

Ma Q, Hu R, Wu Y, Zhang J, Zhi R, Feng G (2022) Variations in July extreme precipitation in Henan Province and the related mechanisms. Int J Climatol 42 (16):9115-9130. doi:10.1002/joc.7805

Mallapaty S (2022) China's extreme weather challenges scientists trying to study it. Nature 609:888. doi:10.1038/d41586-022-02954-8

Marshall GJ (2003) Trends in the Southern Annular Mode from Observations and Reanalyses. J Climate 16 (24):4134-4143. doi:https://doi.org/10.1175/1520-0442(2003)016<4134:TITSAM>2.0.CO;2

Mashat A-WS, Awad AM, Assiri ME, Labban AH (2021) Synoptic pattern of the Red Sea trough associated with spring dust over the northern and western Arabian Peninsula. Meteorol Atmos Phys 133 (3):655-673. doi:10.1007/s00703-020-00771-0

Mishra V, Wallace JM, Lettenmaier DP (2012) Relationship between hourly extreme precipitation and local air temperature in the United States. Geophys Res Lett 39 (16):n/a-n/a. doi:10.1029/2012gl052790

Morice CP, Kennedy JJ, Rayner NA, Winn JP, Hogan E, Killick RE, Dunn RJH, Osborn TJ, Jones PD, Simpson IR (2021) An Updated Assessment of Near-Surface Temperature Change From 1850: The HadCRUT5 Data Set. Journal of Geophysical Research: Atmospheres 126 (3):e2019JD032361. doi:https://doi.org/10.1029/2019JD032361

Nassif WG, Nemah HA, Sada BA (2020) Study of the geopotential height values and its interaction with temperature degree over Baghdad city, Iraq. Plant Archives 20 (2):1388-1391

Nie J, Fang J, Yang X-Q (2022) The mechanisms of the subseasonal zonal oscillation of the western Pacific subtropical high in 10–25-day period and 25–50-day period. Clim Dynam. doi:10.1007/s00382-022-06523-7

Ninomiya K, Kobayashi C (1998) Precipitation and Moisture Balance of the Asian Summer Monsoon in 1991 Part I: Precipitation and Major Circulation Systems. Journal of the Meteorological Society of Japan Ser II 76 (6):855-877. doi:10.2151/jmsj1965.76.6_855

O'Neill BC, Tebaldi C, van Vuuren DP, Eyring V, Friedlingstein P, Hurtt G, Knutti R, Kriegler E, Lamarque JF, Lowe J, Meehl GA, Moss R, Riahi K, Sanderson BM (2016) The Scenario Model Intercomparison Project (ScenarioMIP) for CMIP6. Geoscientific Model Development 9 (9):3461-3482. doi:10.5194/gmd-9-3461-2016

Pedatella NM, Harvey VL (2022) Impact of Strong and Weak Stratospheric Polar Vortices on the Mesosphere and Lower Thermosphere. Geophys Res Lett 49 (10):e2022GL098877. doi:https://doi.org/10.1029/2022GL098877

Po-Chedley S, Santer BD, Fueglistaler S, Zelinka MD, Cameron-Smith PJ, Painter JF, Fu Q (2021) Natural variability contributes to model–satellite differences in tropical tropospheric warming. Proceedings of the National Academy of Sciences 118 (13):e2020962118. doi:10.1073/pnas.2020962118

Polvani LM, Sobel AH (2002) The Hadley Circulation and the Weak Temperature Gradient Approximation. J Atmos Sci 59 (10):1744-1752. doi:https://doi.org/10.1175/1520-0469(2002)059<1744:THCATW>2.0.CO;2

Qiao S, Chen D, Wang B, Cheung HN, Liu F, Cheng J, Tang S, Zhang Z, Feng G, Dong W (2021) The Longest 2020 Meiyu Season Over the Past 60 Years: Subseasonal Perspective and Its Predictions. Geophys Res Lett 48 (9). doi:10.1029/2021gl093596

Rahmstorf S, Coumou D (2011) Increase of extreme events in a warming world. Proceedings of the National Academy of Sciences 108 (44):17905-17909. doi:doi:10.1073/pnas.1101766108

Ramon J, Lledó L, Torralba V, Soret A, Doblas‐Reyes FJ (2019) What global reanalysis best represents near‐surface winds? Q J Roy Meteor Soc 145 (724):3236-3251. doi:10.1002/qj.3616

Rasul G, Chaudhry Q-u-Z, Sixiong Z, Qingcun Z, Linlin Q, Gaoying Z (2005) A diagnostic study of heavy rainfall in Karachi due to merging of a mesoscale low and a diffused tropical depression during South Asian summer monsoon. Adv Atmos Sci 22 (3):375-391. doi:10.1007/bf02918751

Ren D, Dickinson RE, Fu R, Bornman JF, Guo W, Yang S, Leslie LM (2018) Impacts of climate warming on maximum aviation payloads. Clim Dynam 52 (3-4):1711-1721. doi:10.1007/s00382-018-4399-5

Ren G, Wang W, Wan J, Hong F, Yang K, Yu D (2023) Investigating the impacts of spatial-temporal variation features of air density on assessing wind power generation and its fluctuation in China. Science China Technological Sciences 66 (6):1797-1814. doi:10.1007/s11431-022-2248-4

Santer BD, Solomon S, Pallotta G, Mears C, Po-Chedley S, Fu Q, Wentz F, Zou C-Z, Painter J, Cvijanovic I, Bonfils C (2017) Comparing Tropospheric Warming in Climate Models and Satellite Data. J Climate 30 (1):373-392. doi:10.1175/jcli-d-16-0333.1

Sharma AR, Jain P, Abatzoglou JT, Flannigan M (2022) Persistent Positive Anomalies in Geopotential Heights Promote Wildfires in Western North America. J Climate 35 (19):2867-2884. doi:10.1175/jcli-d-21-0926.1

Shaw TA, Voigt A (2015) Tug of war on summertime circulation between radiative forcing and sea surface warming. Nature Geosci 8 (7):560-566. doi:10.1038/ngeo2449

Shi X, Fang Y (2022) Remote forcing effect of sea surface temperatures in the northern tropical Atlantic on tropical cyclone genesis over the Western North Pacific in July. Int J Climatol 42 (7):3666-3680. doi:10.1002/joc.7438

Sickmöller M, Blender R, Fraedrich K (2000) Observed winter cyclone tracks in the northern hemisphere in re-analysed ECMWF data. Q J Roy Meteor Soc 126 (563):591-620. doi:https://doi.org/10.1002/qj.49712656311

Simmons AJ, Berrisford P, Dee DP, Hersbach H, Hirahara S, Thépaut JN (2017) A reassessment of temperature variations and trends from global reanalyses and monthly surface climatological datasets. Q J Roy Meteor Soc 143 (702):101-119. doi:10.1002/qj.2949

Sobel AH, Nilsson J, Polvani LM (2001) The Weak Temperature Gradient Approximation and Balanced Tropical Moisture Waves. J Atmos Sci 58 (23):3650-3665. doi:https://doi.org/10.1175/1520-0469(2001)058<3650:TWTGAA>2.0.CO;2

Stuecker MF, Bitz CM, Armour KC, Proistosescu C, Kang SM, Xie S-P, Kim D, McGregor S, Zhang W, Zhao S, Cai W, Dong Y, Jin F-F (2018) Polar amplification dominated by local forcing and feedbacks. Nat Clim Chang 8 (12):1076-1081. doi:10.1038/s41558-018-0339-y

Su H, Neelin JD, Meyerson JE (2003) Sensitivity of Tropical Tropospheric Temperature to Sea Surface Temperature Forcing. J Climate 16 (9):1283-1301. doi:10.1175/1520-0442-16.9.1283

Sugimoto S, Ueno K (2012) Role of Mesoscale Convective Systems Developed around the Eastern Tibetan Plateau in the Eastward Expansion of an Upper Tropospheric High during the Monsoon Season. Journal of the Meteorological Society of Japan Ser II 90 (2):297-310. doi:10.2151/jmsj.2012-209

Sun S, Li D (2018) Variability in the western Pacific subtropical high and its relationship with sea surface temperature variation considering the background of climate warming over the past 60 years. J Trop Meteorol 24 (4):468-480

Sun X, Ding Q, Wang S-YS, Topál D, Li Q, Castro C, Teng H, Luo R, Ding Y (2022) Enhanced jet stream waviness induced by suppressed tropical Pacific convection during boreal summer. Nature Communications 13 (1). doi:10.1038/s41467-022-28911-7

Takaya Y, Ishikawa I, Kobayashi C, Endo H, Ose T (2020) Enhanced Meiyu ‐ Baiu Rainfall in Early Summer 2020: Aftermath of the 2019 Super IOD Event. Geophys Res Lett 47 (22). doi:10.1029/2020gl090671

Tang S, Qiao S, Wang B, Liu F, Feng T, Yang J, He M, Chen D, Cheng J, Feng G, Dong W (2023) Linkages of unprecedented 2022 Yangtze River Valley heatwaves to Pakistan flood and triple-dip La Niña. npj Climate and Atmospheric Science 6 (1). doi:10.1038/s41612-023-00386-3

Trenberth KE, Smith L (2005) The Mass of the Atmosphere: A Constraint on Global Analyses. J Climate 18 (6):864-875. doi:https://doi.org/10.1175/JCLI-3299.1

Visbeck M (2009) A Station-Based Southern Annular Mode Index from 1884 to 2005. J Climate 22 (4):940-950. doi:https://doi.org/10.1175/2008JCLI2260.1

Wang C, Wang B (2021) Impacts of the South Asian high on tropical cyclone genesis in the South China Sea. Clim Dynam 56 (7-8):2279-2288. doi:10.1007/s00382-020-05586-8

Wang L, Chen W, Zhou W, Huang R (2009) Interannual Variations of East Asian Trough Axis at 500 hPa and its Association with the East Asian Winter Monsoon Pathway. J Climate 22 (3):600-614. doi:10.1175/2008jcli2295.1

Wei W, Zhang R, Wen M, Rong X, Li T (2014) Impact of Indian summer monsoon on the South Asian High and its influence on summer rainfall over China. Clim Dynam 43 (5-6):1257-1269. doi:10.1007/s00382-013-1938-y

Wu L, Wang C (2015) Has the Western Pacific Subtropical High Extended Westward since the Late 1970s? J Climate 28 (13):5406-5413. doi:10.1175/jcli-d-14-00618.1

Yan M, Qian Y, Liu J (2011) Interdecadal variations of the western Pacific subtropical high and surface heat flux over East Asia and their relationship. Acta Meteorol Sin 25 (2):156-165. doi:10.1007/s13351-011-0023-x

Yang B, Chen L, Singh VP, Yi B, Leng Z, Zheng J, Song Q (2023) A Method for Monthly Extreme Precipitation Forecasting with Physical Explanations. Water 15 (8):1545

Yang H, Sun S (2003) Longitudinal displacement of the subtropical high in the western Pacific in summer and its influence. Adv Atmos Sci 20 (6):921-933

Yang J, Peltier WR, Hu Y (2016) Monotonic decrease of the zonal SST gradient of the equatorial Pacific as a function of CO2 concentration in CCSM3 and CCSM4. Journal of Geophysical Research: Atmospheres 121 (18):10,637-610,653. doi:10.1002/2016jd025231

Ying J, Collins M, Cai W, Timmermann A, Huang P, Chen D, Stein K (2022) Emergence of climate change in the tropical Pacific. Nat Clim Chang 12 (4):356-364. doi:10.1038/s41558-022-01301-z

Zhang D, Chen L, Yuan Y, Zuo J, Ke Z (2023) Why was the heat wave in the Yangtze River valley abnormally intensified in late summer 2022? Environmental Research Letters 18 (3):034014. doi:10.1088/1748-9326/acba30

Zhang F, Yang X, Sun Q, Yao S, Guo Q (2022b) Three-Dimensional Structural Anomalies of the Western Pacific Subtropical High Ridge and Its Relationship with Precipitation in China during August–September 2021. Atmosphere 13 (7):1089. doi:10.3390/atmos13071089

Zhang W, Hari V, S‐Y Wang S, LaPlante MD, Garfin G, Affram G, Kumar R (2022a) Fewer Troughs, Not More Ridges, Have Led to a Drying Trend in the Western United States. Geophys Res Lett 49 (1). doi:10.1029/2021gl097089

Zhou C, Wang K (2017) Quantifying the Sensitivity of Precipitation to the Long-Term Warming Trend and Interannual–Decadal Variation of Surface Air Temperature over China. J Climate 30 (10):3687-3703. doi:10.1175/jcli-d-16-0515.1

Zhou T, Ren L, Liu H, Lu J (2018) Impact of 1.5 °C and 2.0 °C global warming on aircraft takeoff performance in China. Science Bulletin 63 (11):700-707. doi:10.1016/j.scib.2018.03.018

Zhou Z-Q, Xie S-P, Zhang R (2021) Historic Yangtze flooding of 2020 tied to extreme Indian Ocean conditions. Proceedings of the National Academy of Sciences 118 (12):e2022255118. doi:10.1073/pnas.2022255118

Table 1 Global averaged value of dH/dT_s at various pressure levels based on the MMM of CMIP6 models and multiple reanalysis datasets (unit: gpm/K). The dH/dT_s values are obtained based on the 1940-2022 period based on the MMM and ERA5 dataset, and the 1980-2022 period based on the NCEP1, NCEP2, JRA55, and MERRA2 datasets.

	MMM	ERA5	NCEP1	NCEP2	JRA55	MERRA2
200 hPa	62.1	53.6	51.2	51.3	48.5	56.6
300 hPa	46.2	41.2	44.9	43.8	41.1	42.6
400 hPa	33.5	30.8	34.7	35.0	32.1	29.6
500 hPa	24.5	23.1	27.0	25.9	25.2	21.6
600 hPa	17.8	17.3	20.0	19.1	19.4	16.5
700 hPa	12.3	12.2	13.5	13.3	14.3	12.0
850 hPa	5.7	6.0	4.6	5.1	8.0	4.6

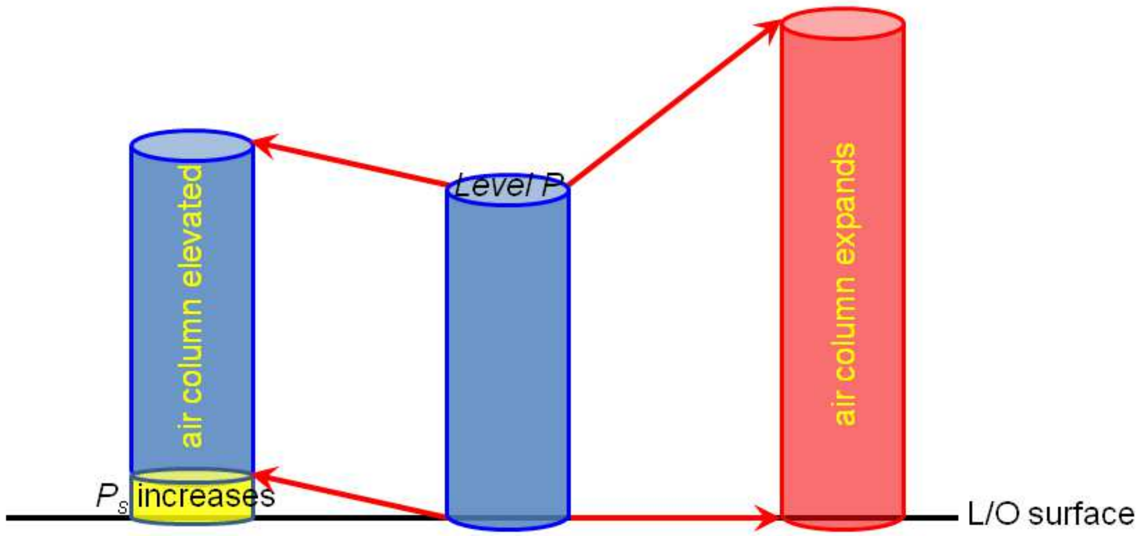

Fig. 1 Schematic illustration of the mechanisms for the increase in H at a given pressure level considering an air column below the pressure level. 1) A rise in surface pressure raises the entire air column, and the height of the top of the air column rises even if the length of the air column is unchanged (left). 2) The length of the air column increases due to reduced air density, which raises the height of the top of the air column.

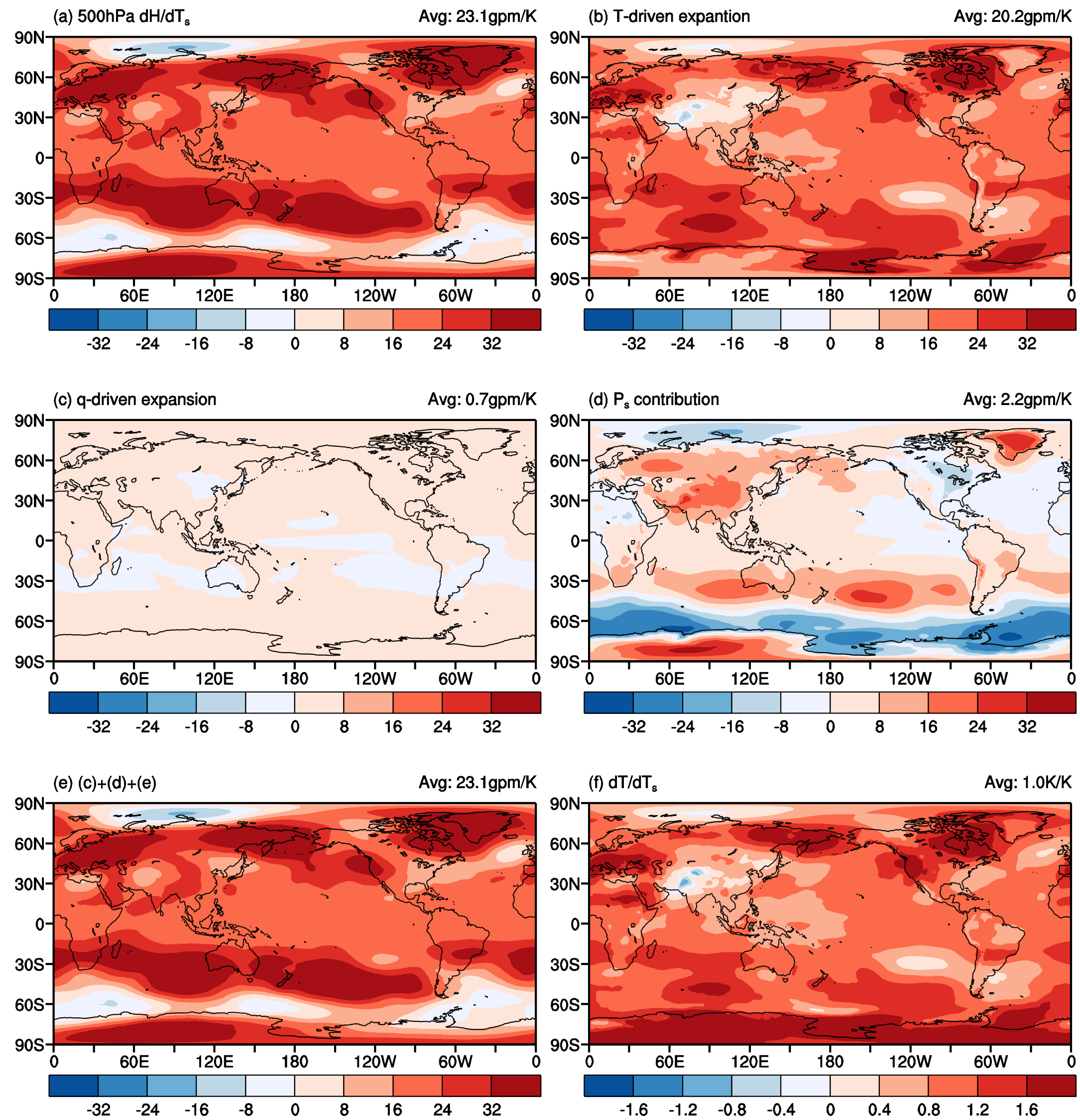

Fig. 2 (a) dH/dT_s at 500 hPa (unit: gpm/K) based on ERA5 data, calculated as the regression slope of H onto the global mean surface air temperature. (b-d) The contributions of T-driven expansion, q-driven expansion, and the P_s effect to dH/dT_s (units: gpm/K). (e) The sum of (b), (c), and (d). (f) The amplitude of air column warming below 500 hPa, calculated as the regression slope of vertically averaged temperature below 500 hPa onto T_s.

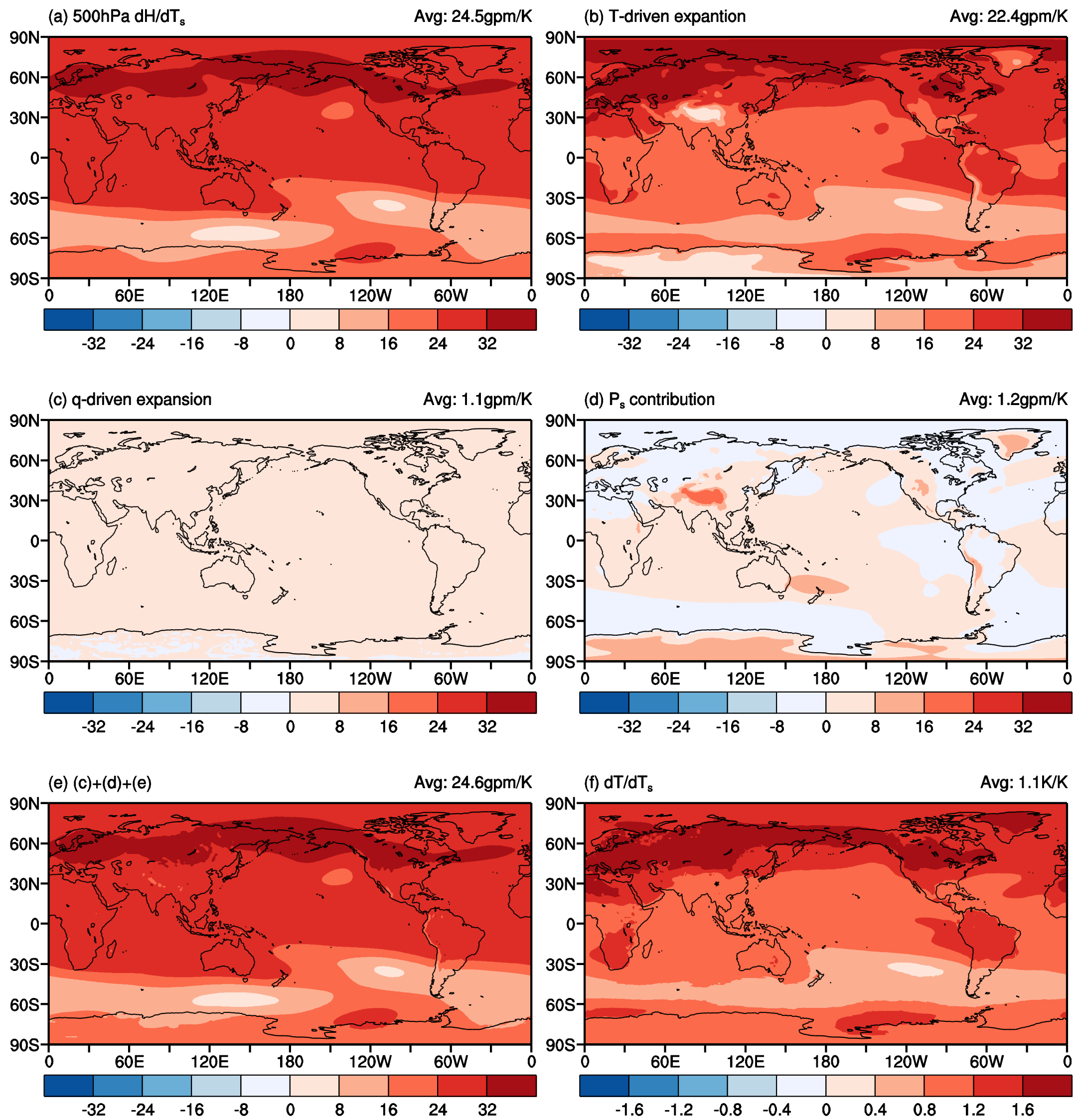

Fig. 3 Same as Fig. 2, but based on the MMM of 40 models participating in CMIP6.

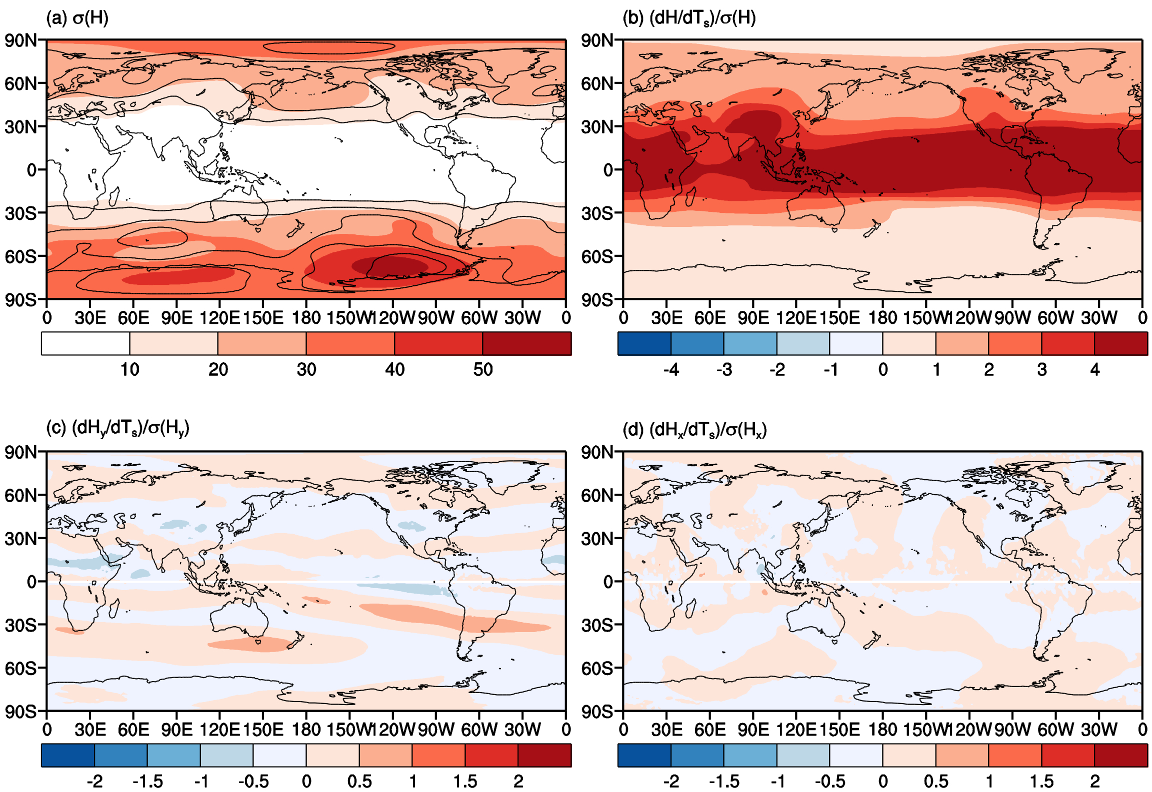

Fig. 4 (a) The interannual standard deviation of H ($\sigma(H)$, unit: gpm) at 500 hPa based on the MMM (shading) and ERA5 data (contour starts at 10 gpm with an interval of 10 gpm). (b) The ratio between $\mathrm{d}H/\mathrm{d}T_s$ and $\sigma(H)$. (c) The ratio between $\mathrm{d}H_y/\mathrm{d}T_s$ and $\sigma(H_y)$. (d) The ratio between $\mathrm{d}H_x/\mathrm{d}T_s$ and $\sigma(H_x)$. Here, H_y and H_x stand for the meridional and zonal gradients of H, which are proportional to the zonal and meridional components of geostrophic wind.

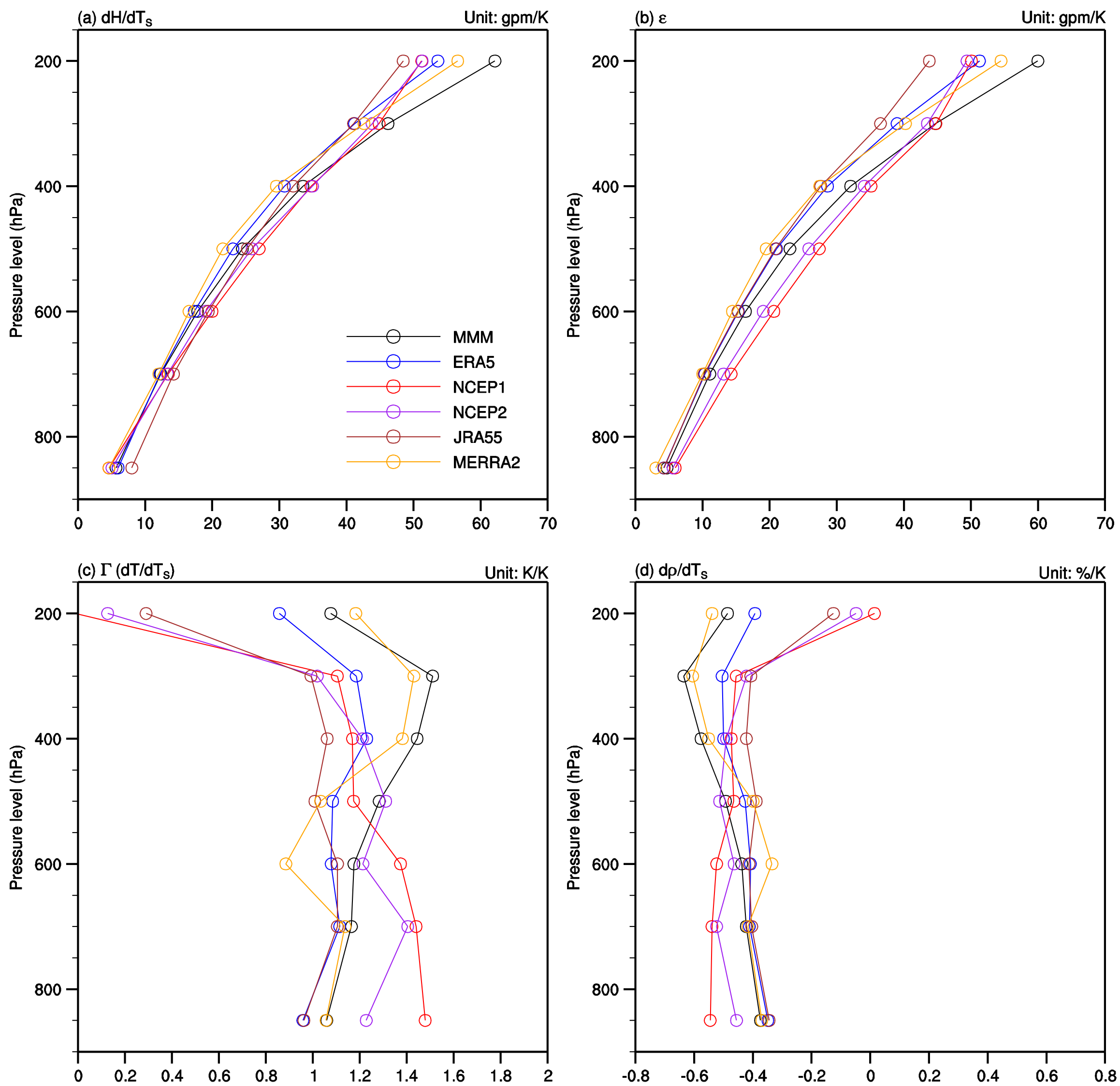

Fig. 5 (a) Global averaged vertical profile of dH/dT_s (unit: gpm/K) based on the MMM (black curve) and reanalysis datasets (colored curves). (b) Estimated dH/dT_s (ε, unit: gpm/K) based on vertical integration of the warming profile according to Eq. (7). (c) Global averaged vertical profile of warming (Γ, unit: K/K) defined as the regression slope of temperature at each pressure level onto T_s. (d) Global averaged vertical profile of fractional change in air density (unit: %/K) defined as the regression slope of fractional change in density onto T_s.

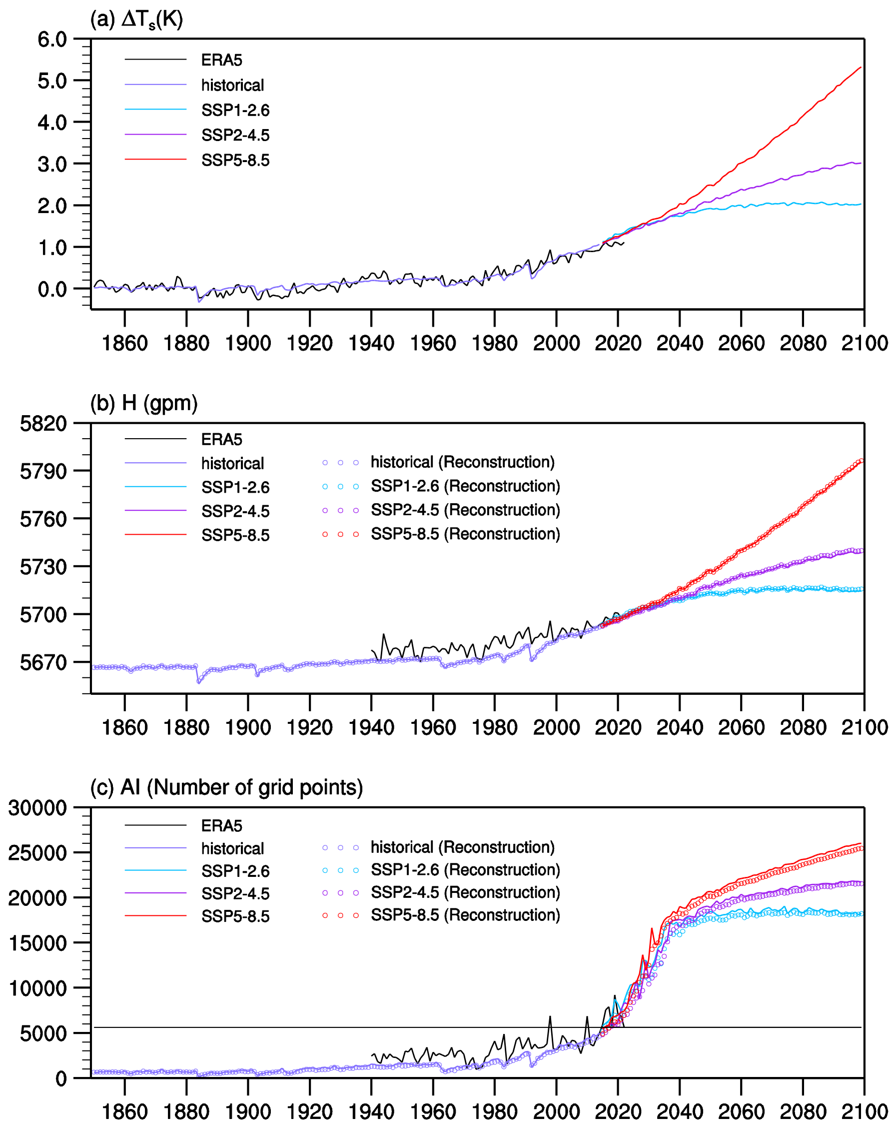

Fig. 6 (a) Time series for the global mean surface air temperature anomaly (ΔT_s, unit: K) relative to the 1850-1899 baseline period. (b) Time series for global mean H at 500 hPa (unit: gpm, curves) and reconstructed H (hollow circles). (c) Time series for the area index (AI, curves), defined as the number of grid points with H above 5880 gpm, and the reconstructed AI (hollow circles). The reconstructed H field in one year is obtained by adding a global uniform value of $24.5\Delta T_s$ to the climatological H field of the baseline period.

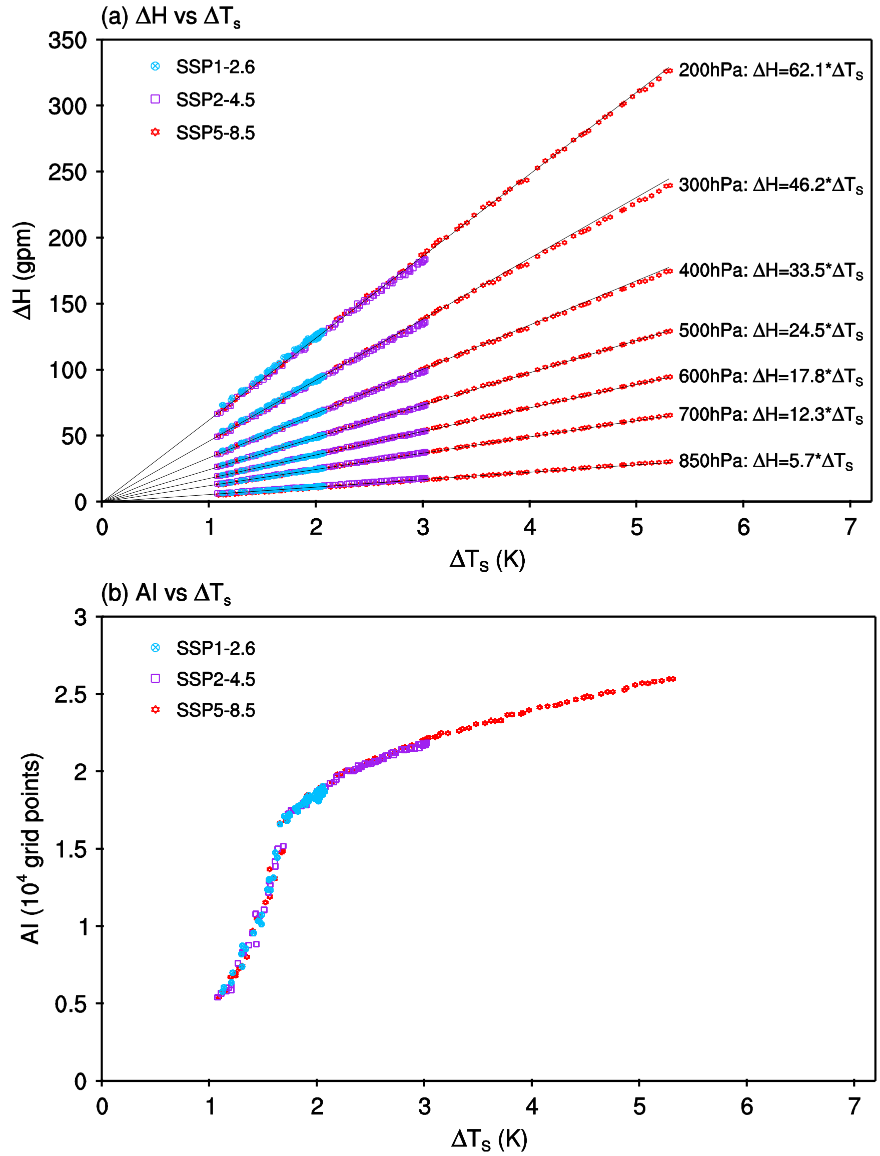

Fig. 7 (a) The MMM-projected change in H (ΔH) as a function of ΔT_s in each year from 2015 to 2099 based on the SSP1-2.6, SSP2-4.5, and SSP5-8.5 scenarios, relative to the 1850-1899 baseline of the historical experiment. The black lines in (a) indicate the $\Delta H = k\Delta T_s$ lines where k is the dH/dT_s value at each pressure level listed in Table 1. (b) The MMM-projected change in AI (number of grid points with an H value above 5880 gpm) as a function of ΔT_s in each year from 2015 to 2099 based on the three scenarios, calculated as (5880-H)/24.5 (unit: K)

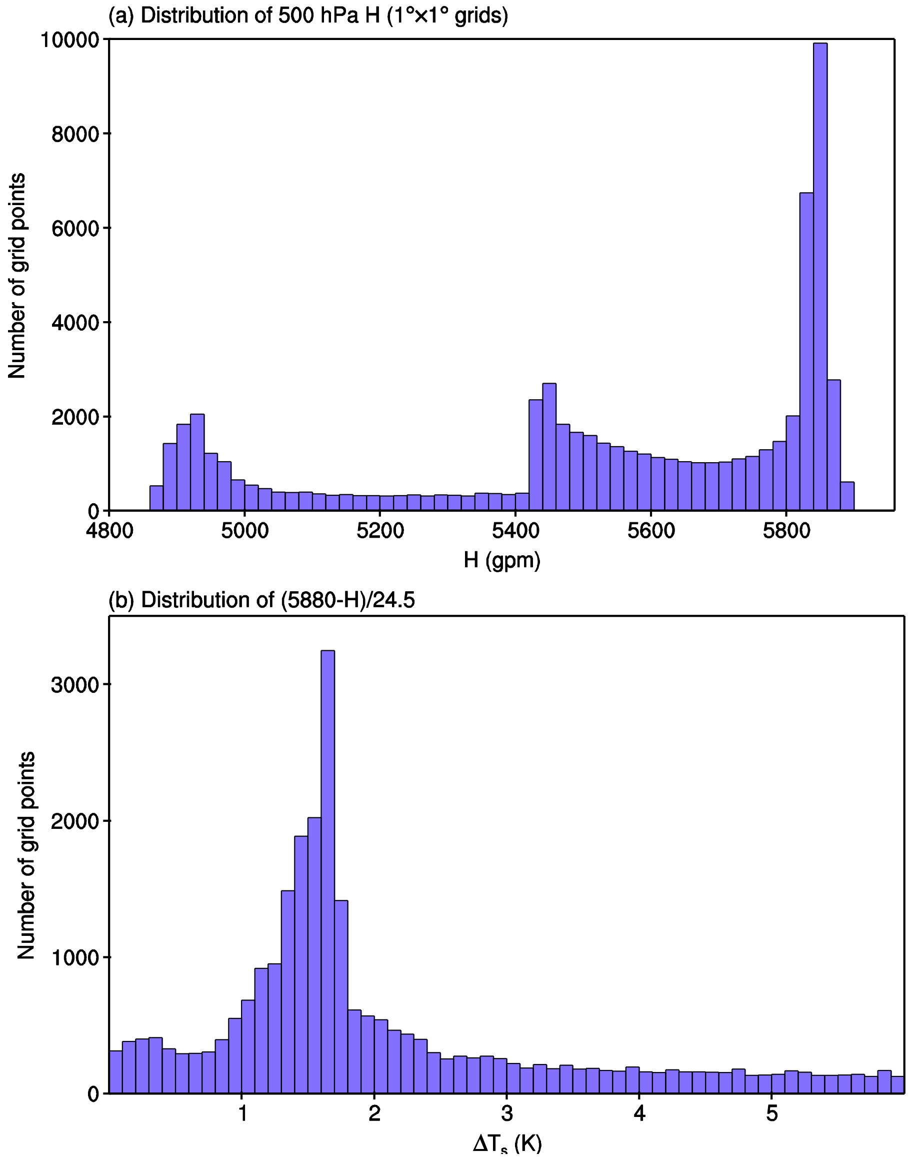

Fig. 8 (a) Distribution of climatological H values at 500 hPa for global grid points at a 1°×1° resolution, based on the baseline period (1850-1899 average) of the MMM. (b) Distribution of (5880−H)/24.5 at 500 hPa for global grid points, which indicates the amplitude of ΔT_s required for the H value of grid points to reach 5880 gpm assuming a global uniform rise in H of 24.5 gpm/K.

Supplementary Files

This is a list of supplementary files associated with this preprint. Click to download.

- SI202309251.pdf